

Characterizing and Mitigating Flux Crosstalk in Superconducting Qubits-Couplers System

Chen-Hsun Ma,^{1,2,*} Myrron Albert Callera Aguila,^{3,*} Nien-Yu Li,^{1,2,*} Li-Chieh Hsiao,³ Yi-Shiang Huang,¹ Yen-Chun Chen,³ Teik-Hui Lee,³ Chin-Chia Chang,¹ Jyh-Yang Wang,⁴ Ssu-Yen Huang,² Hsi-Sheng Goan,^{2,5,6} Chiao-Hsuan Wang,^{2,5,6} Cen-Shawn Wu,^{7,3} Chii-Dong Chen,^{1,3} and Chung-Ting Ke^{1,3,†}

¹*Institute of Physics, Academia Sinica, Nankang, Taipei, 11529, Taiwan*

²*Department of Physics, National Taiwan University, Da'an District, Taipei 10617, Taiwan*

³*Research Center for Critical Issues, Academia Sinica, Guiren, Tainan, 711010, Taiwan*

⁴*Department of Electrical Engineering, Feng-Chia University, Xitun, Taichung 407301, Taiwan*

⁵*Center for Quantum Science and Engineering, National Taiwan University, Taipei 106319, Taiwan*

⁶*Physics Division, National Center for Theoretical Sciences, Taipei 106319, Taiwan*

⁷*Department of Physics, National Changhua University of Education, Changhua, Changhua 500207, Taiwan*

(Dated: August 6, 2025)

Superconducting qubits have achieved exceptional gate fidelities, exceeding the error-correction threshold in recent years. One key ingredient of such improvement is the introduction of tunable couplers to control the qubit-to-qubit coupling through frequency tuning. Moving toward fault-tolerant quantum computation, increasing the number of physical qubits is another step toward effective error correction codes. Under a multiqubit architecture, flux control (Z) lines are crucial in tuning the frequency of the qubits and couplers. However, dense flux lines result in magnetic flux crosstalk, wherein magnetic flux applied to one element inadvertently affects neighboring qubits or couplers. This crosstalk obscures the idle frequency of the qubit when flux bias is applied, which degrades gate performance and calibration accuracy. In this study, we characterize flux crosstalk and suppress it in a multiqubit-coupler chip with multi-Z lines without adding additional readout for couplers. By quantifying the mutual flux-induced frequency shifts of qubits and couplers, we construct a cancellation matrix that enables precise compensation of non-local flux, demonstrating a substantial reduction in Z-line crosstalk from 56.5‰ to 0.13‰ which is close to statistical error. Flux compensation corrects the CZ SWAP measurement, leading to a symmetric map with respect to flux bias. Compared with a crosstalk-free calculated CZ SWAP map, the measured map indicates that our approach provides a near-zero crosstalk for the coupler-transmon system. These results highlight the effectiveness of our approach in enhancing flux crosstalk-free control and supporting its potential for scaling superconducting quantum processors.

Keywords: Superconducting qubits, Quantum Physics, Quantum Information

Superconducting qubits are one of the promising types of physical qubits to realize fault-tolerant quantum computing (FTQC), in which quantum computers tackle problems that conventional computers cannot solve on a reasonable time scale [1, 2]. In operating high-fidelity quantum gates, the tunable coupler plays a crucial role. It suppresses spurious coupling and modulates the coupling strength between two qubits [3–5] via coupler-mediated virtual exchange [1, 4]. These features enhance single-qubit (1Q) and two-qubit (2Q) gate fidelities in both transmon and fluxonium architectures [6, 7] in a superconducting quantum processor. Reaching the error correction threshold marks the first step towards FTQC [1, 8–10].

To achieve FTQC, an increasing number of qubits and couplers is needed, which leads to more control lines as well as crosstalk between qubits and couplers. Crosstalks could originate from unintended microwave [11–14] and readout drives [15, 16], residual qubit-to-qubit cou-

pling [3, 4, 6, 17], frequency crowding [5, 18–20], and unwanted flux [21–24] that leads to imperfection of the 1Q and 2Q gates. Flux crosstalk plays a role in a frequency-tunable qubit-coupler system; it obscures the precise frequency detuning required for a quantum gate operation. Precise control of the flux pulse avoids unwanted frequency shifts and residual coupling, which is beneficial for quantum gate operation.

In a transmon-coupler (TC) architecture [1, 4–6], flux control relies on the current flowing through a flux (Z) line grounded near the qubit or coupler. As depicted in Fig. 1(a), four flux lines, colored green and labeled Z, are responsible for frequency control with flux threading through the superconducting quantum interference device (SQUID) loop. To characterize flux crosstalk in the TC system, we utilize the tunable two-qubit and two-coupler system, as shown in Fig. 1(a). Here, the element referring to the flux line i , $k \in \{Z_{Q1}, Z_{Q2}, Z_{C1}, Z_{C2}\}$ interacts with an element referring to the SQUID loop of a target qubit or coupler $j \in \{Q1, Q2, C1, C2\}$. When the current I_i generated by a voltage difference V_i across a load impedance of $50\ \Omega$ passes through a target flux line antenna, I_i induces two effects that generate flux crosstalk: 1) residual inductive coupling $L_{ij, i \neq j}$ between flux lines

* C.-H. M., M. A. C. A. and N.-Y. L. contributed equally in the manuscript

† ctke@as.edu.tw

and SQUID loops of neighboring qubits and couplers and 2) unwanted fluxes threading through SQUIDs due to return currents [23, 25]. Flux crosstalk complicates the precise control of TC system for quantum gate operations.

To overcome the crosstalk challenge, we develop a protocol for characterizing flux crosstalk in a compact TC architecture that exploits residual inductive coupling between several flux-tunable elements to resolve the 0-1 transition frequencies of the probed element, named "Multi-Z-Line Control" (MZLC). The method only requires prior knowledge of the flux bias dependence of the qubit/coupler spectrum. It is independent on the readout fidelity and applies to arbitrary flux biases of the probed element. We apply this method in compact TC with dense wiring of flux lines without a dedicated readout resonator and drive line for coupler. MZLC reveals average flux crosstalk of $26.5 \pm 18.7\%$ and $0.2 \pm 0.14\%$, before and after the flux crosstalk matrix compensation. Flux crosstalk matrix cancellation after MZLC enables the coupler-assisted coupling strength to be symmetric with varying coupler detuning after compensation, easing up the tune-up of conditional-phase (CZ) gates.

The protocol for characterizing flux crosstalk is carried out on a subsystem of a quantum processing unit (QPU) containing five qubits and four couplers, as shown in Figs. 1(b). The QPU is fabricated with conventional e-beam lithography, followed by a tilt-angle deposition of aluminum with in situ oxidation to make the circuit elements and Manhattan-style Josephson junctions. The MZLC protocol is implemented in a TC subsystem located at the edge of the linear qubit chain, as shown in Figs. 1(b) and 1(c). Wire bonds are placed above the microwave and flux lines to suppress slot line modes [26], and flux crosstalk [25]. The experiment is conducted in a dilution refrigerator with a base temperature of 10 mK, and the microwave signal is supplied by Quantum Machines OPX+ (see [27] for additional details).

Figures 1(c) and 1(d) show the magnified image of the flux-tunable TC subsystem and its lumped circuit diagram with matching color schemes. The TC subsystem consists of two Xmon qubits (labeled Q) and a double C-shaped coupler (labeled C), all with flux lines. Each qubit has a microwave drive line and a readout resonator (labeled R) coupled to a shared Purcell filter. The frequencies of the resonators f_R , qubits $f_{01,Q}$ and couplers $f_{01,C}$ are arranged so that $f_{01,C} > f_R > f_{01,Q}$, as noted in Table S2 of the supplemental material [27]. The neighboring flux lines between the qubit and the coupler have a distance of $250\text{ }\mu\text{m}$, shown in Fig. 1(c). This distance affects crosstalk and residual couplings, which is expected in superconducting qubit-coupler processors with dense wiring, as shown in Fig. 1(d).

Next, we detail the protocol for characterizing the crosstalk of the TC system. Figures 2(a) and 2(b) show standard two-tone spectroscopy pulse schedules for qubits and couplers, respectively, with the same color codes as Figs. 1. Figures 2(c) and 2(e) reveal the frequency spectrum of the qubits Q1 and Q2, with the driv-

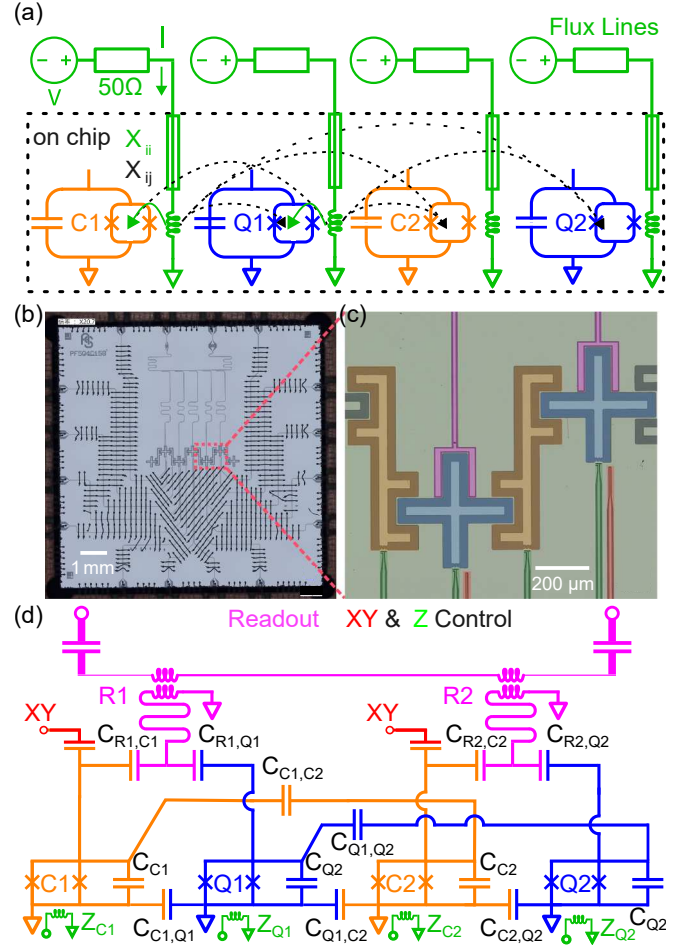


FIG. 1. Subsystem used to characterize magnetic flux crosstalk. (a) Illustration of flux crosstalk. Magnetic flux from the Z-lines causes unwanted frequency shifts of nearby tunable elements. (b) Optical micrograph of the chip, which has five flux-tunable transmon qubits with readout resonators and four flux-tunable couplers. (c) Optical micrograph of the subsystem consisting of two qubits (Q1, Q2) in blue and two couplers (C1, C2) in orange. Color labels are assigned based on the corresponding components in the subsystem's lumped circuit model shown in (d).

ing frequency f_{XY} as a function of the flux bias voltage V_i .

Due to the absence of dedicated readout resonators and XY lines for the couplers, we employ *indirect coupler spectroscopy* (ICS) with the pulse sequence shown in (b). ICS exploits the weak capacitive coupling between the coupler electrode and the XY and readout lines of the adjacent qubits to resolve $f_{01,C}$ [28, 29]. Figs. 2(d) and 2(f) shows the frequency spectra of couplers C1 and C2, respectively. In obtaining Figs. 2(d) and 2(f), the coupler is driven with elevated amplitude of microwave and readout tones to better resolve the 0-1 transition spectrum. Moreover, adding appropriate delay to overlapping drive and readout pulses enhances the contrast of the 0-

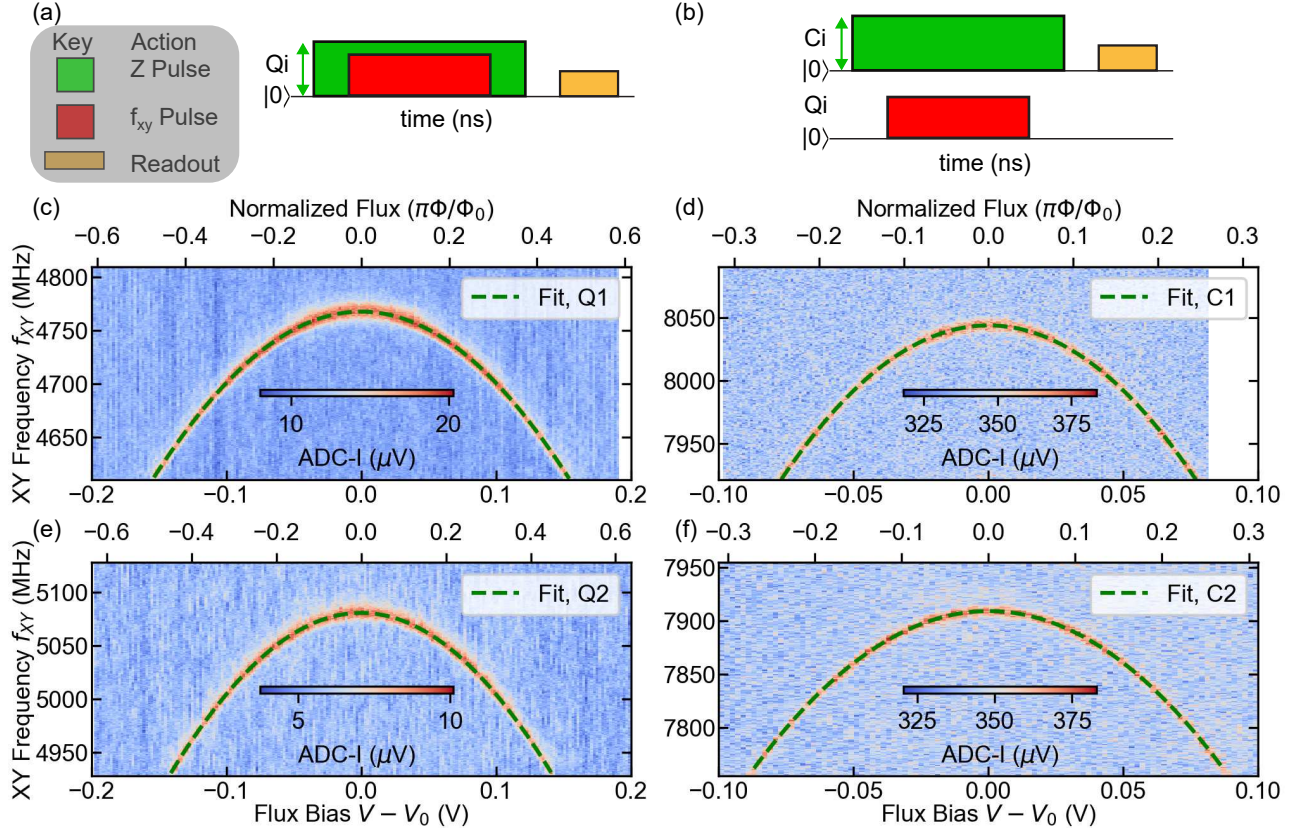


FIG. 2. Qubit and coupler spectrum as a function of flux bias. (a) represents pulse sequences in (c) and (e) to probe qubit's f_{01} , using each qubit's flux bias (green), microwave drive f_{XY} (red) and readout pulse (gold) as noted in the gray box. (c) represents the pulse sequences in (d) and (f) used for the coupler where the flux bias came from the coupler while the microwave and readout drives came from an adjacent qubit and resonator. We probe the qubit and coupler spectrum as a function of the flux shown in (c,e) and (d,f) for qubits and couplers, respectively. Green dashed lines refer to the fit of the f_{01} transition frequencies with the flux-tunable transmon model. The top and bottom horizontal axes refer to the normalized flux bias and applied voltage, respectively.

1 transition in the coupler spectrum, thereby improving the signal-to-noise ratio for both qubit spectroscopy and ICS. As these weak capacitive couplings are inherent in the subsystem design, ICS is compatible with standard measurement schemes.

Sweeping the microwave drive frequency f_{XY} of the qubits' XY line with fixed XY drive and flux bias reveals a peak frequency response with a Lorentzian profile of both the qubits and couplers. The peak frequency, representing the 0-1 transition, changes with flux bias voltage V_i , and follows f_{01} of the flux-tunable transmon model, which is shown as green dashed lines in Figs. 2(a) and 2(d). The model is written as [23, 30]

$$f_{01}(V_i) = \left(f_{01,\max} + \frac{E_C}{h} \right) \times \sqrt{d^2 + [1 - d^2] \cos^2(A_c [V_i - V_{\text{ofs},i}])} - \frac{E_C}{h}, \quad (1)$$

where $f_{01,\max}$ is the upper sweet spot frequency, $-E_C/h$ is the anharmonicity, d is the junction asymmetry, A_c

is a conversion factor related to the mutual inductance between the i^{th} SQUID loop and the i^{th} flux line, and $V_{\text{ofs},i}$ is the offset voltage induced by the remnant flux. Notably, A_c and $V_{\text{ofs},i}$ are related to the normalized flux of the transmon by $A_c(V_i - V_{\text{ofs},i}) = \pi\Phi/\Phi_0$ where Φ is the total flux that traverses the SQUID loop and Φ_0 is the flux quanta. The transmon anharmonicities are determined by two-photon excitation measurements. The junction asymmetries for both qubits and couplers are based on the nominal design in [27]. Hence, A_c , $f_{01,\max}$ and $V_{\text{ofs},i}$ are extracted when fitting the model with the driven spectra in Figs. 2(c) and (f), expressed in voltages from the analog-to-digital converter in-phase channel (ADC-I) [31]. These parameters map the idle transmon frequency to its corresponding flux bias [30], and vice versa after flux crosstalk compensation (see [27] for details).

We then investigate the flux crosstalk for the qubits and couplers. Figures 3(a) shows the pulse sequence of the MZLC protocol with a similar legend in Fig. 2(a). In principle, an arbitrary flux pulse duration can work for MZLC. To maintain consistency, we set the initialization

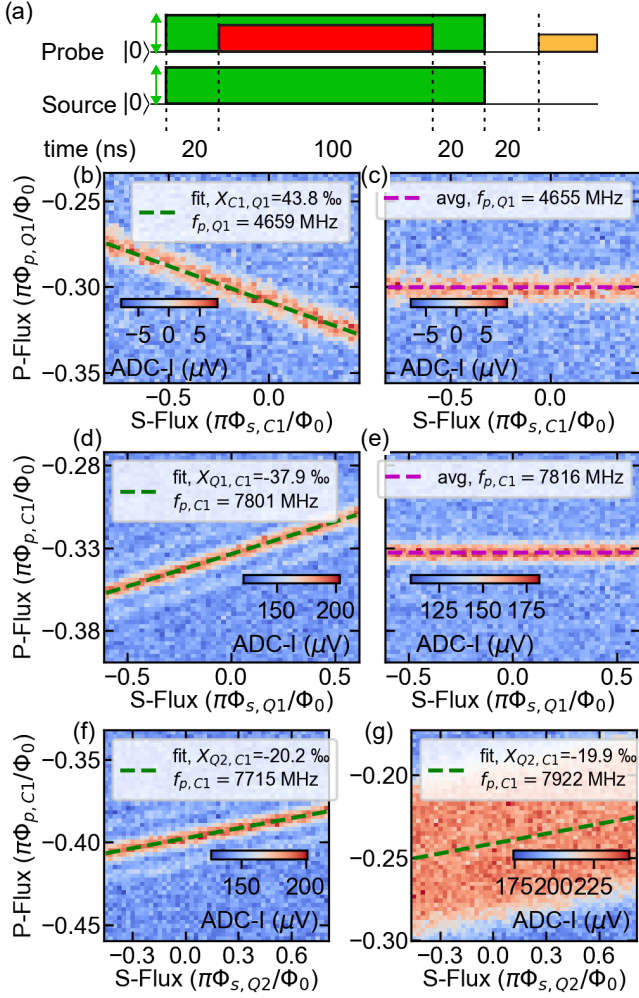


FIG. 3. Characterization of flux crosstalk. (a) Pulse sequence used to extract crosstalk of MZLC: a probing element is driven at a fixed frequency, while both probe voltage and source voltage are applied simultaneously. The π_{01} , Z, and readout pulses have 20 ns delays to avoid timing mismatch artifacts. Spectra with crosstalk are illustrated in intensity plots with C1 as source and Q1 as probe (b) and vice versa (d). The horizontal, vertical, and intensity axes are the source flux (S-Flux), probe flux (P-Flux), and readout signal voltage, respectively. Applying flux-compensated pulses to (b) and (d) after characterizing the flux crosstalk results in spectra immune to S-Flux as shown in (c) and (e), respectively. As the probe qubit is detuned near its sweet spot, it affects the spectral linewidth with Q2 as a source and C1 as a probe. All measurement conditions are identical, except in (f) where the probe element is biased 0.1 V away from its sweet spot (g).

time to 200 μ s, and set both the flux pulse duration and the microwave drive pulse duration to 100 ns throughout the study. Therefore, we can ensure that the crosstalk X_{ik} , where i and k are flux lines and $i \neq k$, is not affected by variations in the pulse configuration.

Figures 3(b) and 3(d) show crosstalk measurement results using MZLC. The horizontal and vertical axes represent the applied voltage on the source and probe flux

lines, respectively, which are converted to flux quanta, named S-Flux ($\pi\Phi_{s,i}/\Phi_0$) and P-flux ($\pi\Phi_{p,i}/\Phi_0$). Each data point represents a frequency response (f_{01}) of the qubits (couplers) as a detector under a fixed driving frequency and a simultaneous bias of the source and probe elements. We set a 20 ns delay between pulses to reduce the transient time effect of the flux pulse. The scheme hinges on detecting flux crosstalk by observing undesirable frequency shifts on the detector induced by S-Flux. It is worth noting that an alternative method is the Ramsey-based method, which observes the same sign and magnitude of crosstalk, as shown in Fig. 4(b) and Fig. S2 of the supplemental material [27]. Within the S-flux ranges shown in Figs. 3(b) and (d), the f_{01} of the probe elements are linearly proportional to the flux quanta of the source element, implying linear crosstalk between neighboring flux-controlled elements. We model this linear dependence on the source frequency $f_{s,i}$ as

$$f_{p,k} = X_{ik}f_{s,i} + f_{p,i} = \frac{-\Delta V_{p,k}}{\Delta V_{s,i}}f_{s,i} + f_{p,i}, \quad (2)$$

where $X_{ik} = -\Delta V_{p,k}/\Delta V_{s,i}$ is the flux crosstalk coefficient obtained from the slope of Figs. 3(b) and 3(d). We label X_{ik} as the non-diagonal elements of the flux crosstalk matrix X along with its normalized diagonal term ($X_{ii} = 1$). With X measured, one can calculate the inverse matrix, which leads to a cancellation matrix X^{-1} . After applying X^{-1} to reconfigure our flux pulses, the remeasured flux crosstalk maps in Figs. 3(c) and 3(e) show that the S-Flux does not affect on the transition frequency of the probe element. The results not only support the validity of Eq. (2) but also confirm a significant suppression of flux crosstalk. Notably, the intercept $f_{p,i}$ extracted from Figs. 3(b) and 3(d) is a good estimate of the probe idle frequency $f_{p,k}$ after flux compensation, as shown in Figs. 3(c) and 3(e). We attribute these megahertz discrepancies to uncorrected long-time-scale transients of the flux pulses [6, 17, 32].

When using the MZLC approach, detuning the probe element away from its upper sweet spot leads to a narrow linewidth, which improves the precision of flux crosstalk measurement, as shown in Fig. 3(f). Conversely, detuning the probe element towards the upper sweet spot frequencies as shown in Fig. 3(g), results in a broadened spectral linewidth and larger error bar in the crosstalk fitting. These linewidths are consistent with the qubit and coupler spectra in Figs. 2, which are observed in previous works [6, 33–36].

Two possible mechanisms explain the broadening observed in Fig. 3(f) and 3(g). First, sweeping S-Flux is equivalent to scanning an attenuated P-flux on the qubit spectrum due to stray mutual inductance, which induces spectrum broadening around the sweet spot. Second, the amplitude of the second tone is not fine-tuned while changing the frequency of the detector, which modifies the transmon spectrum outside the sweet spot. Nonetheless, the sign and amplitude of the crosstalk in Figs. 3(f) and 3(g) remain unchanged.

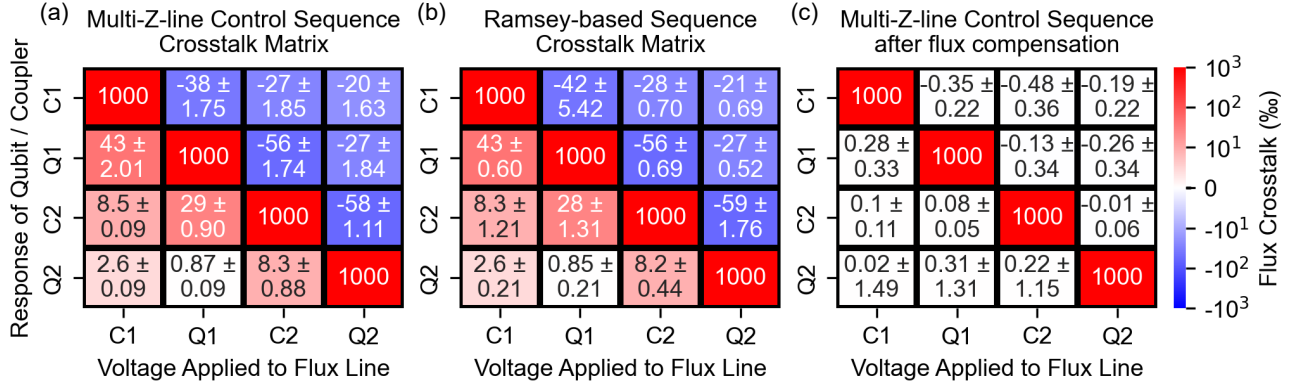


FIG. 4. Flux crosstalk matrices between tunable elements. Rows correspond to detector elements, and columns to source Z-lines. (a) Displaying results obtained from two-tone spectroscopy averaged over 100 repetitions to estimate statistical uncertainty. (b) shows corresponding results from Ramsey, which agrees with statistical error to (a). (c) show the crosstalk matrix after compensation, demonstrating suppression of all off-diagonal elements to below 0.5 %.

TABLE I. Metrics for Flux Crosstalk X_{ik} (in %) before and after flux crosstalk compensation based on Figs. 4(a) and (c)

Metric	Notation	Before	After
Largest Negative	$\text{Min}(X_{ik})$	-58.0 ± 1.11	-0.48 ± 0.36
Largest Positive	$\text{Max}(X_{ik})$	43.0 ± 2.01	0.31 ± 1.31
Average	$\langle X_{ik} \rangle_{i \neq k}$	26.5 ± 18.7	0.20 ± 0.14
Total	$\sum_{i \neq k} X_{ik} $	318.4	2.42
Matrix	$\sum_{i \neq k}$	143.6	0.94
Asymmetry	$ X_{ik} - X_{ki} $		

We summarize the crosstalk matrices measured using the MZLC and Ramsey sequences in Figs. 4(a) and 4(b), respectively. Both methods yield consistent results within the statistical error. Table I shows the statistical properties of X_{ik} before and after flux compensation in Figs. 4(a) and 4(c), respectively. A few observations of the crosstalk matrix are as follows. First, the average uncompensated crosstalk has the same order as its extreme values (Fig. S3 of [27] presents the same results in dB). Its total crosstalk is similar to previous flux-tunable two-qubit transmons [37]. Its matrix asymmetry exhibits an imbalance likely stemming from the leftward routing layout of our flux lines, producing asymmetric inductive coupling and return current. A careful routing of flux lines [25] with the return current flowing directly on the PCB ground [38] could passively reduce the flux crosstalk and matrix asymmetry to a certain extent. Lastly, these metrics dropped one to two orders of magnitude after flux compensation; residual crosstalk averages near zero, with a standard deviation of a similar scale. The flux-compensated crosstalk becomes decoupled, uniform, and reciprocal.

In addition to compensating for flux crosstalk, we applied this method to help locate the optimal bias point for conditional phase (CZ) gate operations [6, 17, 39]. In TC architectures, the coupler-mediated CZ gate works by tuning the frequencies of the qubits so that the states

$|11\rangle$ and $|20\rangle$ become resonant, resulting in a state swap. The effective coupling strength g_{eff} in this regime is susceptible to detuning between the frequencies of qubits and couplers, which in turn depends on the applied flux bias.

We show measured coupler-tuned CZ SWAP experiments using the pulse schedule in Fig. 5(a). The behavior seen in Figs. 5(b) and 5(c) before and after flux compensation, respectively. To compare with Fig. 5(d), it is derived from the Rabi oscillation for 2Q gates [36, 40] accounting for the finite rising time of the diabatic flux pulse (see additional details of the model from [27]). Due to phase errors arising from the uncalibrated pulse distortions in flux biasing [17, 41], Figs. 5(b) and 5(c) may show a small deviation from Fig. 5(d).

As finite resolution in Figs. 5(b) and 5(c) prevent us to extract the coupling strength via FFT like in other works [42, 43], we fit the readout signals representing the $|11\rangle$ population versus time duration in Figs. 5(b) and 5(c) with a cosine function to extract the effective coupling strengths $\Omega = \sqrt{4g_{\text{eff}}^2 + \delta_{21}^2}$, where g_{eff} is the coupler-mediated coupling strength for the CZ gate, δ_{21} is the detuning between the $|11\rangle$ and $|02\rangle$ states. Using the extracted qubit and coupler parameters in another chip with identical circuit design using Eq. (1), we determined $\delta_{21}/2\pi = 9.33$ MHz. After subtracting the CZ detuning from Ω , we extracted $|g_{\text{eff}}|$ as a function of the flux of the coupler C_2 , shown in Fig. 5(e), for both compensated and uncompensated cases.

The CZ coupling strength in a TC architecture (Q1-C2-Q2) is written as [42, 43]

$$g_{\text{eff}} = \sqrt{2} \left(g_{12} - \frac{g_{1c}g_{2c}}{2} B_{02} \right), \quad (3)$$

where g_{12} is the direct coupling between Q1 and Q2, g_{1c} is the coupling strength between Q1 and coupler C2, g_{2c} is the coupling strength between Q2 and coupler C2, and

$$B_{02} = \frac{1}{\Delta_1} + \frac{1}{\Delta_2 - E_{C,2}/\hbar} + \frac{1}{\sum_1} + \frac{1}{\sum_2 + E_{C,2}/\hbar}, \quad (4)$$

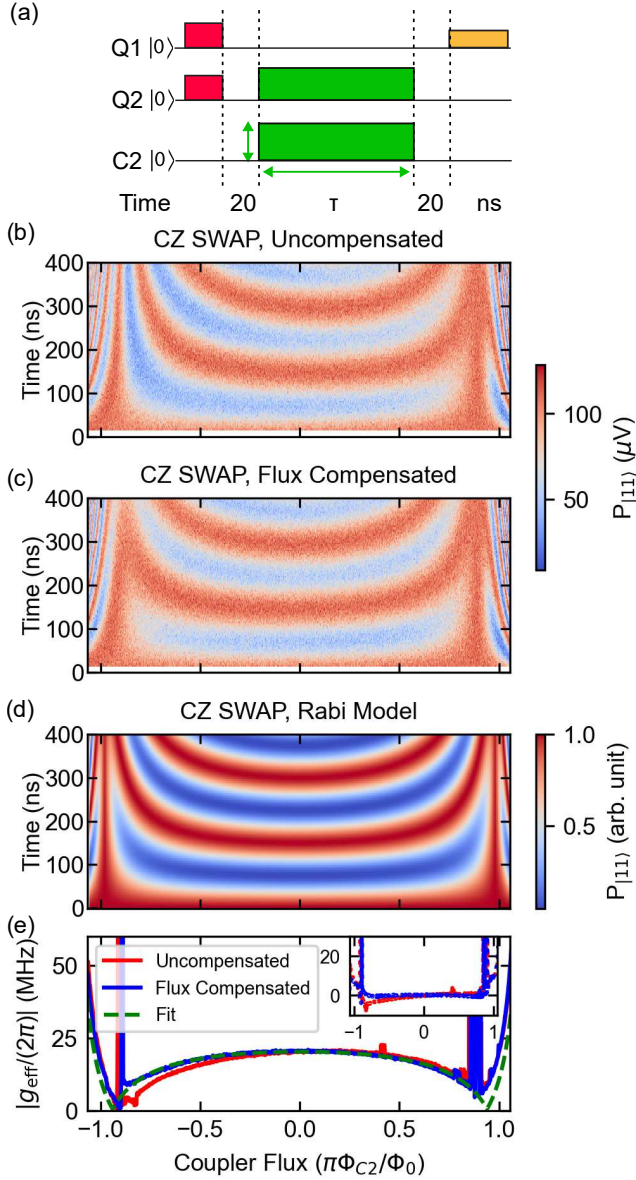


FIG. 5. Time-domain measurements of the coherent oscillations between $|11\rangle$ (red) and $|02\rangle$ (blue) states, named CZ SWAP, under varying coupler flux and different flux pulse durations. The pulse schedule in (a), and the results before flux compensation (b) and after flux compensation (c) are displayed. The flux-compensated time-domain measurements agree with simulations in (d). (e) 2D Fast Fourier transform (FFT) of the time-domain oscillations in (b), (c), and (d), which quantifies the conditional phase-mediated coupling strength $|g_{\text{eff}}|$ as a function of coupler flux. Inset shows the residuals (dotted lines) expressed in MHz. Panels from (b) to (e) share the same x-axis, representing the applied flux on the coupler.

where $\Delta_1/2\pi = f_{01,C2} - f_{01,Q1}$ and $\Delta_2/2\pi = f_{01,C2} - f_{01,Q2}$ are the frequency detunings between the coupler and the qubits, and $\Sigma_1/2\pi = f_{01,C2} + f_{01,Q1}$ and $\Sigma_2/2\pi = f_{01,C2} + f_{01,Q2}$ are the frequency sums of the transition frequencies. To fit the flux-compensated

$|g_{\text{eff}}|$ in Fig. 5(e), we use Eqs. (3)–(4) with an added coupling strength of $|435|$ kHz, which could be reduced through better readout fidelity and rigorous flux pre-distortions [17, 40, 41]. The inset in Fig. 5(e) accentuates the effect of flux compensation on predicting $|g_{\text{eff}}|$. At $|\Phi_{C2}| < 0.88\Phi_0$, uncompensated flux pulses generate asymmetric $|g_{\text{eff}}|$ with megahertz offsets from the fit, whereas compensated flux pulses produce predictable $|g_{\text{eff}}|$.

Non-idealities in Fig. 5(e) and its inset become evident when comparing the measured $|g_{\text{eff}}|$ with the fit at $|\Phi_{C2}| \geq 0.88\Phi_0$. The fit cannot explain the sharp peaks at $|g_{\text{eff}}/2\pi|$ at $|\Phi_{C2}| \approx 0.88\Phi_0$ ($f_{C2} \approx 5.94$ GHz) as the predicted singularities occur beyond the range of the coupler flux displayed in Fig. 5(e) [43]. The singularities probably come from the strong coupling between the readout resonator R2 and the coupler C2 as $f_{C2} \approx f_{R2}$ (see [27] for details), which produces hybridized modes as exploited in other works [44, 45]. Hybridization of modes adds difficulty in nulling $|g_{\text{eff}}|$, which explains the monotonic increase in the two residuals when $|\Phi_{C2}| > 0.88\Phi_0$.

The findings in Figs. 5 imply that flux crosstalk compensation creates a magnetic flux crosstalk-free digital twin of the coupler-mediated CZ gate based on empirical adjustments of the Rabi oscillation model [6, 40, 46]. This digital twin helps identify non-idealities in two-qubit gates such as flux transients [6, 32, 40] and unintended hybridization of the qubit and coupler modes. Shaping the flux pulse to account for flux transients [6, 32, 40] while avoiding frequencies that invoke unwanted hybridization of modes [44] could help to match the digital twin with experimental results. We consider the proposed measurement, modeling, and analysis protocol to be suitable for scaling to thousands of qubits with the aid of high-performance computing [2].

In this work, we develop the MZLC protocol for characterizing flux crosstalk in a TC architecture. The method exploits residual inductive coupling between several flux-tunable elements to resolve the 0-1 transition frequencies of the probed element. Whereas other flux crosstalk characterization strategies use Rabi spectroscopy [21, 23, 25] and Ramsey sequences on a single-biased element to characterize the flux crosstalk matrix, relying on the readout fidelity of the qubit/coupler. MZLC has the advantage of characterizing flux crosstalk even in low readout SNR and an arbitrary idle flux bias range. The method requires knowledge of the dependence of the qubit/coupler spectrum on flux bias, which is routine in the bring-up of superconducting processors, making the MZLC a simple, time-efficient tool for characterizing the flux crosstalk matrix of a transmon-coupler subsystem and optimizing CZ gate operation points. Lastly, compared with the CZ SWAP model, the experimental result shows a nearly identical map with zero crosstalk. Therefore, it provides a way to create a digital twin for the TC system CZ optimization.

ACKNOWLEDGMENT

We acknowledge funding support from the Academia Sinica Grand Challenge project (AS-GCP-112-M01), National Quantum Initiative (AS-KPQ-111-TQRB), and NSTC (113-2119-M-001-008). C.-T. K. acknowledges the funding support from NSTC 2030 Cross-Generation Young Scholars(112-2628-M-001-004). H.-S. Goan acknowledges support from the National Science and Technology Council (NSTC), Taiwan, under Grants No. NSTC 113-2112-M-002-022-MY3, and No. 114-2119-M-002-018, and from the National Taiwan University un-

der Grants No. NTU-CC-114L8950, and No. NTU-CC114L895004.

C.-D. C. and C.-T. K. conceived the devices and supervised the project with contributions from H.-S. G., S.-Y. H. and C.-H. W.. C.-C. C. and J.-Y. W. designed the device layout with additional inputs from T.-H. L. Y.-C. C. coordinated the device fabrication. Y.-C. C., C.-S. W., C.-D. C., and C.-T. K. provided input on the fabrication methodology. N.-Y. L., L.-C. H. and Y.-S. H. conducted the experiment. C.-H. M., M.A.C.A., N.-Y. L., L.-C. H., and C.-T. K. analyzed the data and wrote the manuscript; all authors discussed the results and contributed to the manuscript.

-
- [1] F. Arute, K. Arya, R. Babbush, D. Bacon, J. C. Bardin, R. Barends, R. Biswas, S. Boixo, F. Brandao, D. A. Buell, et al., *Nature* **574**, 505 (2019).
 - [2] M. Mohseni, A. Scherer, K. G. Johnson, O. Wertheim, M. Otten, N. A. Aadit, Y. Alexeev, K. M. Bresniker, K. Y. Camsari, B. Chapman, et al., *How to build a quantum supercomputer: Scaling from hundreds to millions of qubits* (2025), [arXiv:2411.10406 \[quant-ph\]](#).
 - [3] Y. Chen, C. Neill, P. Roushan, N. Leung, M. Fang, R. Barends, J. Kelly, B. Campbell, Z. Chen, B. Chiaro, et al., *Phys. Rev. Lett.* **113**, 220502 (2014).
 - [4] F. Yan, P. Krantz, Y. Sung, M. Kjaergaard, D. L. Campbell, T. P. Orlando, S. Gustavsson, and W. D. Oliver, *Phys. Rev. Appl.* **10**, 054062 (2018).
 - [5] J. Stehlik, D. M. Zajac, D. L. Underwood, T. Phung, J. Blair, S. Carnevale, D. Klaus, G. A. Keefe, A. Carniol, M. Kumph, et al., *Phys. Rev. Lett.* **127**, 080505 (2021).
 - [6] Y. Song, L. Ding, J. Braumüller, A. Vepsäläinen, B. Kannan, M. Kjaergaard, A. Greene, G. O. Samach, C. McNally, D. Kim, et al., *Phys. Rev. X* **11**, 021058 (2021).
 - [7] L. Ding, M. Hays, Y. Sung, B. Kannan, J. An, A. Di Paolo, A. H. Karamlou, T. M. Hazard, K. Azar, D. K. Kim, et al., *Phys. Rev. X* **13**, 031035 (2023).
 - [8] N. Lacroix, A. Bourassa, F. J. H. Heras, L. M. Zhang, J. Bausch, A. W. Senior, T. Edlich, N. Shuttly, V. Sivak, A. Bengtsson, et al., *Nature* (2025), published online, doi:10.1038/s41586-025-09061-4.
 - [9] R. Acharya, D. A. Abanin, L. Aghababaie-Beni, I. Aleiner, T. I. Andersen, M. Ansmann, F. Arute, K. Arya, A. Asfaw, N. Astrakhantsev, et al., *Nature* **638**, 920 (2025).
 - [10] D. Gao, D. Fan, C. Zha, J. Bei, G. Cai, J. Cai, S. Cao, F. Chen, J. Chen, K. Chen, et al., *Phys. Rev. Lett.* **134**, 090601 (2025).
 - [11] R. Wang, P. Zhao, Y. Jin, and H. Yu, *Appl. Phys. Lett.* **121**, 152602 (2022).
 - [12] H. Yan, S. Zhao, Z. Xiang, Z. Wang, Z. Yang, K. Xu, Y. Tian, H. Yu, D. Zheng, H. Fan, et al., *Chin. Phys. B* **32**, 094203 (2023).
 - [13] Z. H. Yang, R. Wang, Z. T. Wang, P. Zhao, K. Huang, K. Xu, Y. Tian, H. F. Yu, and S. P. Zhao, *Appl. Phys. Lett.* **124**, 214001 (2024).
 - [14] X.-Y. Yang, H.-F. Zhang, L. Du, H.-R. Tao, L.-L. Guo, T.-L. Wang, Z.-L. Jia, W.-C. Kong, Z.-Y. Chen, P. Duan, et al., *Appl. Phys. Lett.* **125**, 044001 (2024).
 - [15] J. Heinsoo, C. K. Andersen, A. Remm, S. Krinner, T. Walter, Y. Salathé, S. Gasparinetti, J.-C. Besse, A. Potočník, A. Wallraff, et al., *Phys. Rev. Appl.* **10**, 034040 (2018).
 - [16] D. Pitsun, A. Sultanov, I. Novikov, E. Mutsenik, B. Ivanov, A. Matanin, V. Polozov, E. Malevannaya, A. Ivanov, G. Fedorov, et al., *Phys. Rev. Appl.* **14**, 054059 (2020).
 - [17] R. Li, K. Kubo, Y. Ho, Z. Yan, Y. Nakamura, and H. Goto, *Phys. Rev. X* **14**, 041050 (2024).
 - [18] J. B. Hertzberg, E. J. Zhang, S. Rosenblatt, E. Magesan, J. A. Smolin, J.-B. Yau, V. P. Adiga, M. Sandberg, M. Brink, J. M. Chow, et al., *NPJ Quantum Inf.* **7**, 129 (2021).
 - [19] E. J. Zhang, S. Srinivasan, N. Sundaresan, D. F. Bogorin, Y. Martin, J. B. Hertzberg, J. Timmerwille, E. J. Pritchett, J.-B. Yau, C. Wang, et al., *Sci. Adv.* **8**, 1 (2022).
 - [20] D. P. Pappas, M. Field, C. J. Kopas, J. A. Howard, X. Wang, E. Lachman, J. Oh, L. Zhou, A. Gold, G. M. Stiehl, et al., *Commun. Mater.* **5**, 150 (2024).
 - [21] R. Barends, J. Kelly, A. Megrant, A. Veitia, D. Sank, E. Jeffrey, T. C. White, J. Mutus, A. G. Fowler, B. Campbell, et al., *Nature* **508**, 500 (2014).
 - [22] C. Neill, P. Roushan, K. Kechedzhi, S. Boixo, S. V. Isakov, V. Smelyanskiy, A. Megrant, B. Chiaro, A. Dunsworth, K. Arya, et al., *Nature* **360**, 195 (2018).
 - [23] C. N. Barrett, A. H. Karamlou, S. E. Muschinske, I. T. Rosen, J. Braumüller, R. Das, D. K. Kim, B. M. Niedzielski, M. Schuldt, K. Serniak, et al., *Phys. Rev. Appl.* **20**, 024070 (2023).
 - [24] X. Dai, R. Trappen, R. Yang, S. M. Disseler, J. I. Basham, J. Gibson, A. J. Melville, B. M. Niedzielski, R. Das, D. K. Kim, et al., *Quantum Sci. Tech.* **9**, 025007 (2024).
 - [25] S. Kosen, H.-X. Li, M. Rommel, R. Rehammar, M. Caputo, L. Grönberg, J. Fernández-Pendás, A. F. Kockum, J. Biznárová, L. Chen, et al., *PRX Quantum* **5**, 030350 (2024).
 - [26] J. Wenner, M. Neeley, R. C. Bialczak, M. Lenander, E. Lucero, A. D. O'Connell, D. Sank, H. Wang, M. Weides, A. N. Cleland, et al., *Supercond. Sci. Technol.* **24**, 065001 (2011).
 - [27] (2025), see Supplemental Material at [URL] for experimental and theoretical details.
 - [28] X. Li, T. Cai, H. Yan, Z. Wang, X. Pan, Y. Ma, W. Cai,

- J. Han, Z. Hua, X. Han, et al., *Phys. Rev. Appl.* **14**, 024070 (2020).
- [29] M. C. Collodo, J. Herrmann, N. Lacroix, C. K. Andersen, A. Remm, S. Lazar, J. C. Besse, T. Walter, A. Wallraff, and C. Eichler, *Phys. Rev. Lett.* **125**, 240502 (2020).
- [30] J. Koch, T. M. Yu, J. Gambetta, A. A. Houck, D. I. Schuster, J. Majer, M. H. Blais, Alexander; Devoret, S. M. Girvin, and R. J. Schoelkopf, *Phys. Rev. A* **76**, 042319 (2007).
- [31] D. Sank, A. Opremcak, A. Bengtsson, M. Khezri, Z. Chen, O. Naaman, and A. Korotkov, *Phys. Rev. Appl.* **23**, 024055 (2025).
- [32] T.-M. Li, J.-C. Zhang, B.-J. Chen, K. Huang, H.-T. Liu, Y.-X. Xiao, C.-L. Deng, G.-H. Liang, C.-T. Chen, Y. Liu, et al., *Phys. Rev. Appl.* **23**, 024059 (2025).
- [33] D. I. Schuster, A. Wallraff, A. Blais, L. Frunzio, R. S. Huang, J. Majer, S. M. Girvin, and R. J. Schoelkopf, *Phys. Rev. Lett.* **94**, 123602 (2005).
- [34] H. Paik, D. I. Schuster, L. S. Bishop, G. Kirchmair, G. Catelani, A. P. Sears, B. R. Johnson, M. J. Reagor, L. Frunzio, L. I. Glazman, et al., *Phys. Rev. Lett.* **107**, 240501 (2011).
- [35] J. D. Whittaker, F. C. S. da Silva, M. S. Allman, F. Lecocq, K. Cicak, A. J. Sirois, J. D. Teufel, J. Aumentado, and R. W. Simmonds, *Phys. Rev. B* **90**, 024513 (2014).
- [36] A. V. Anferov, *Millimeter Wave Superconducting Quantum Devices* (2024), PhD Thesis, University of Chicago.
- [37] J. M. Chow, *Quantum information processing with superconducting qubits* (2010), PhD Thesis, Yale University.
- [38] Z. Niu, W. Gao, X. He, Y. Wang, Z. Wang, and Z.-R. Lin, *Appl. Phys. Lett.* **124**, 254002 (2024).
- [39] B. Foxen, C. Neill, A. Dunsworth, P. Roushan, B. Chiaro, A. Megrant, J. Kelly, Z. Chen, K. Satzinger, R. Barends, et al., *Phys. Rev. Lett.* **125**, 120504 (2020).
- [40] C. Hellings, N. Lacroix, A. Remm, R. Boell, J. Herrmann, S. Lazar, S. Krinner, F. Swiadek, C. K. Andersen, C. Eichler, et al., *Calibrating Magnetic Flux Control in Superconducting Circuits by Compensating Distortions on Time Scales from Nanoseconds up to Tens of Microseconds* (2025), [arXiv:2503.04610 \[quant-ph\]](#).
- [41] Y. H. Shi, R. Q. Yang, Z. Xiang, Z. Y. Ge, H. Li, Y. Y. Wang, K. Huang, Y. Tian, X. Song, D. Zheng, et al., *Nat. Commun.* **14**, 3263 (2023).
- [42] E. A. Sete, N. Didier, A. Q. Chen, S. Kulshreshtha, R. Manenti, and S. Poletto, *Phys. Rev. Appl.* **16**, 024050 (2021).
- [43] G.-H. Liang, X.-H. Song, C.-L. Deng, X.-Y. Gu, Y. Yan, Z.-Y. Mei, S.-L. Zhao, Y.-Z. Bu, Y.-X. Xiao, Y.-H. Yu, et al., *Phys. Rev. Appl.* **20**, 044028 (2023).
- [44] L. Chen, S. P. Fors, Z. Yan, A. Ali, T. Abad, A. Osman, E. Moschandreou, B. Lienhard, S. Kosen, H.-X. Li, et al., *Fast unconditional reset and leakage reduction in fixed-frequency transmon qubits* (2024), [arXiv:2409.16748 \[quant-ph\]](#).
- [45] X. Zhang, X. Zhang, C. Chen, K. Tang, K. Yi, K. Luo, Z. Xie, Y. Chen, and T. Yan, *Characterization and optimization of tunable couplers via adiabatic control in superconducting circuits* (2025), [arXiv:2501.13646 \[quant-ph\]](#).
- [46] C. Križan, J. Biznárová, L. Chen, E. Hogedal, A. Osman, C. W. Warren, S. Kosen, H.-X. Li, T. Abad, A. Aggarwal, et al., *New J. Phys.* **27**, 074507 (2025).

Supplemental Material for "Characterizing and Mitigating Flux Crosstalk in Superconducting Qubits-Couplers System"

Chen-Hsun Ma,^{1,2} Myrron Albert Callera Aguila,³ Nien-Yu Li,^{1,2} Li-Chieh Hsiao,³ Yi-Shiang Huang,¹ Yen-Chun Chen,³ Teik-Hui Lee,³ Chin-Chia Chang,¹ Jyh-Yang Wang,⁴ Ssu-Yen Huang,² Hsi-Sheng Goan,^{2,5,6} Chiao-Hsuan Wang,^{2,5,6} Cen-Shawn Wu,^{7,3} Chii-Dong Chen,^{1,3} and Chung-Ting Ke^{1,3}

¹*Institute of Physics, Academia Sinica, Nankang, Taipei, 11529, Taiwan*

²*Department of Physics, National Taiwan University, Da'an District, Taipei 10617, Taiwan*

³*Research Center for Critical Issues, Academia Sinica, Guiren, Tainan, 711010, Taiwan*

⁴*Department of Electrical Engineering, Feng-Chia University, Xitun, Taichung 407301, Taiwan*

⁵*Center for Quantum Science and Engineering, National Taiwan University, Taipei 106319, Taiwan*

⁶*Physics Division, National Center for Theoretical Sciences, Taipei 106319, Taiwan*

⁷*Department of Physics, National Changhua University of Education, Changhua, Changhua 500207, Taiwan*

(Dated: August 6, 2025)

I. DEVICE FUNDAMENTALS

We fabricated the device on a high-resistivity (100) Si substrate ($\rho = 10 \text{ k}\Omega \text{ cm}$) based on a 4-inch wafer process. We first performed a UV ozone cleaning process for two minutes, followed by a hydrofluoric acid "HF" dip to remove native oxides on the substrate for one minute, and then rinsing with deionized water (DIW). The N_2 -dried wafer is baked at 200°C in a vacuum before spin coating with electron beam resist. A 100 kV e-beam writer defines all circuit elements prior to resist development. We then transfer the patterned wafer to conduct conventional double-angle evaporation, forming a Manhattan junction as well as other superconducting regions. The thickness of Al is 50 nm and 100 nm for the first and second layers, respectively. Lastly, we do a gentle resist lift-off and cleaning process to remove the resist, metal and organic residues. An automatic wire-bonder is used to tie the ground planes on the chip to reduce flux crosstalk [1].

TABLE S1. Simulated Parameters for Qubits and Couplers in the CZ idle configuration ($f_R = 6.0 \text{ GHz}$, $f_{Q1,\text{idle}} = 4931 \text{ MHz}$, $f_{Q2,\text{idle}} = 4789 \text{ MHz}$, $f_{C1,\text{idle}} = 7735 \text{ MHz}$ and $f_{C2,\text{idle}} = 5379 \text{ MHz}$) based on Ansys Q3D simulations

Transmon	C1	C2	Q1	Q2
E_C/h (MHz)	153	153	206	206
$g_{qr}/2\pi$ (MHz)	8.10	13.4	106	111
$g_{R1,R2}/2\pi$ (MHz)	-	-	1.98	1.98

The e-beam pattern layout is drawn using the KLayout software. Ansys Q3D is used to calculate the self-capacitance and coupling capacitance of the circuit layout. These capacitances translate into target charging energies and resonator-qubit coupling strengths based on previous works[2, 3], as listed in Table S1. Notably, the calculation of the resonator-resonator coupling strength serves as the weakest coupling magnitude in the subsystem.

The lithographic areas of the SQUIDs for qubits and couplers have distinct designs. The square junction areas

of the SQUIDs of our qubits are nominally asymmetric ($A_{Q,j1} = 0.07 \times 0.07 \mu\text{m}^2$, $A_{Q,j2} = 0.152 \times 0.152 \mu\text{m}^2$). The square junction areas for the couplers are nominally symmetric, although with different widths ($A_{C,j1} = A_{C,j2} = 0.228 \times 0.228 \mu\text{m}^2$). The Josephson energy is written as

$$E_J = \frac{\Phi_0 \Delta}{4eR_N} \tanh \frac{\Delta}{2k_B T}, \quad (\text{S1})$$

where Φ_0 is the magnetic flux quantum, e is the electron charge, $k_B T$ is the thermal energy, and Δ is the superconducting energy gap of aluminum. We define the normal state resistance $R_N = R_J/A$ [4], where R_J is the junction resistance per unit area and A is the junction area. Hence, we get a relation of $E_J \propto A$. For asymmetric junctions, the junction asymmetry d of the transmons is written as

$$d = \frac{\gamma - 1}{\gamma + 1}, \quad (\text{S2})$$

where $\gamma = E_{J2}/E_{J1}$. Based on the designed areas of the junctions in the qubits, $\gamma_Q = A_{Q,j2}/A_{Q,j1} = 4.715$, and the junction asymmetry of the qubits is $d_Q = 0.65$. For symmetric junctions of the coupler SQUIDs, $d_C = 0$. These values of d are integral in confirming the parameters of the qubit and coupler spectra, as noted in the latter section and in the main text.

II. MEASUREMENT WIRING AND EXPERIMENTAL TUNEUP

The chip, which contains the quantum processing unit (QPU), has five qubits and four Transmon Couplers (TC) that are arranged in a linear array. Each qubit has its dedicated $\lambda/4$ coplanar waveguide (CPW) resonators, with a shared $\lambda/2$ CPW to ensure fast readout (RO). Typical readout resonator frequencies are around 5.9 – 6.1 GHz. The chip is mounted on a single-layer tin-plated PCB board with a small sliver of GE varnish on the bottom part of the chip to provide thermal link with

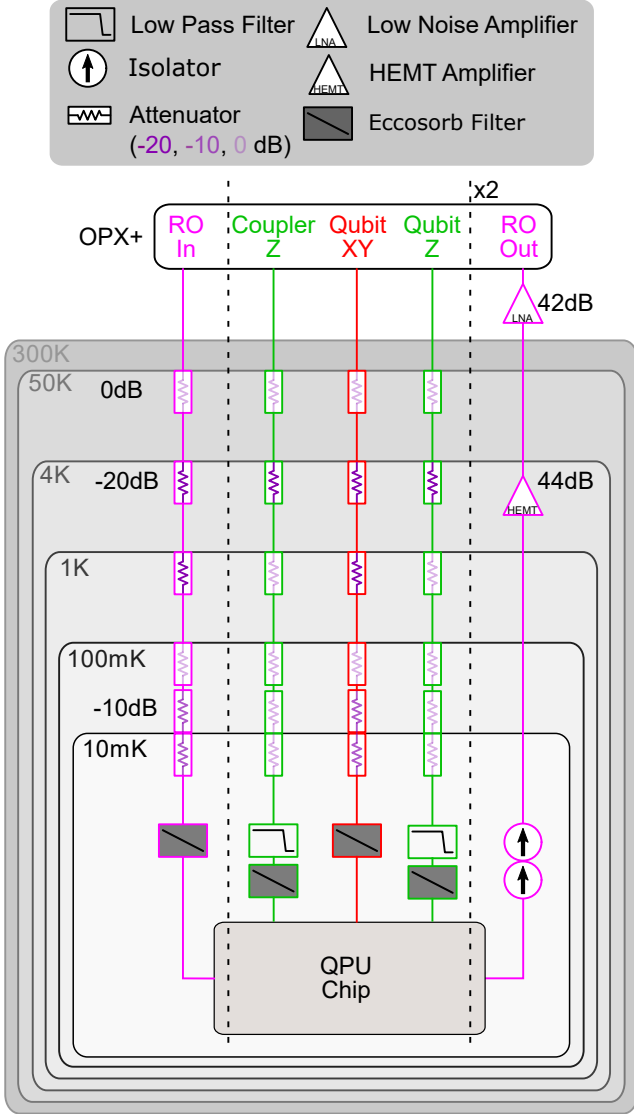


FIG. S1. Wiring schematic of the measurement setup. Different resistor colors in the attenuator refer to the attenuation level (see legend). Colored lines refer to the qubit readout (RO, magenta), microwave drive (XY, red) and flux (Z, green) control noted in Figs. 1(c,d) of the main text. Dashed lines refers to region in the measurement setup that has duplicated wiring and control for multiple qubits and couplers.

the base temperature of the dilution fridge (DR). Aluminum wire bonds connect the signal and readout lines of the chip to the 50 ohm electrodes of the PCB board [5]. The PCB board is covered with an aluminum cap followed by a mu-metal cap to attenuate the magnitude of trapped flux [6].

The chip mount is tightly screwed onto an Au-plated copper plate for thermalization of the Bluefors LD-400 DR, as shown in Fig. S1. The 0-dB attenuators thermally connect the inner conductor of the cables to different stage plates of the DR. Both readout (RO-in) and microwave drive (Qubit-XY) lines have similar attenua-

tors to minimize the population of the qubit with thermal photons [7]. Superconducting coaxial cables connect the SMA connectors between 4 K and 10 mK for the flux lines (Coupler Z and Qubit Z), and output readout lines (RO-out), as shown in Fig. S1. A dissipative 500-MHz low-pass filter (LPF) is used to damp high-frequency standing waves that may be created when applying baseband pulses between the flux line antenna and the low-pass filter [6]. Eccosorb filters are connected to the readout, microwave drive, and flux lines to minimize stray IR radiation coming from the SMA connectors. The measured voltage signals from the readout resonators are amplified by a series of low-noise amplifiers, and are upconverted with IQ mixers.

TABLE S2. Physical Parameters of the Transmon-Coupler System

Transmon	C1	Q1	C2	Q2
f_r (MHz)	6073.7 ± 0.2		5985.8 ± 0.2	
$f_{01,\max}$ (MHz)	8044.6	4768.6	7909.3	5081.9
	± 0.2	± 0.5	± 1.5	± 0.5
$g_{qr}/2\pi$ (MHz)	3.6 ± 1.3	93.9 ± 2.0	1.5 ± 0.2	94.7 ± 1.5
E_C/h (MHz)	119.8	206.2	127.2	207.6
	± 2.8	± 2.8	± 2.8	± 2.8
T_1 (μ s)	4.8 ± 0.4	11.1 ± 0.5	4.9 ± 0.9	6.0 ± 0.6
T_2 (μ s)	7.1 ± 1.6	4.8 ± 0.4	4.0 ± 0.6	8.0 ± 0.6
$^1T_2^R$ (μ s)	2.3 ± 1.8	2.4 ± 0.2	3.3 ± 0.4	2.1 ± 0.1
2F_a (%)	83.9	90.1	72.4	91.6

¹ Ramsey T_2 time

² F_a refers to readout assignment fidelity.

Our 1Q gate tune-up follows standard calibration protocols for flux-tunable transmon qubits [8] to characterize the device parameters. Both microwave and flux pulses are generated using the RF and arbitrary waveform generator ports of the Quantum Machines OPX+ pulse processing unit. A Gaussian pulse with gate duration of 20 ns is used to excite the qubit to its $|1\rangle$ and obtain the relaxation time T_1 , and dephasing time T_2^R by the Rabi and Ramsey pulse sequences, respectively. Readout assignment fidelities are optimized by single-shot measurements with a 4 μ s integration time. 1Q gate fidelities of 99.6 % for Q1 and Q2 were obtained with the microwave drive with derivative removal by the adiabatic gate (DRAG) sequence. A rectangular flux pulse with 100 ns gate duration is used to tune the qubit frequency. Both microwave and flux pulses were used to perform two-tone spectroscopy, as shown in Figs. 2 and 3 of the main text. Other relevant parameters of the devices that are not discussed in the main text are listed in Table S2.

III. CALIBRATION BETWEEN FLUX AND QUBIT-COUPLER INTERACTIONS

A. Mapping between Flux Bias Voltage and Transmon Idle Frequency

The frequency of a flux-tunable qubit (or coupler), which has a SQUID loop as a tunable element, is governed by its Josephson energy E_J , which depends on the external magnetic flux Φ . In the transmon limit ($E_J \gg E_C$), the $0 \rightarrow 1$ transition frequency of the flux-tunable qubits and couplers f_{01} can be written as[9]

$$f_{01}(\Phi) = \frac{\sqrt{8E_J E_C}(\Phi) - E_C}{h}, \quad (\text{S3})$$

with

$$E_J(\Phi) \rightarrow E_{J,\max} \cos\left(\frac{\pi\Phi}{\Phi_0}\right) \sqrt{1 + d^2 \tan^2 \frac{\pi\Phi}{\Phi_0}}, \quad (\text{S4})$$

where $E_{J1,\max} = E_{J1} + E_{J2}$ is the sum of energies of two junctions in a SQUID loop, $d = (E_{J2} - E_{J1})/E_{J,\max}$ is the junction asymmetry, and E_C is the charging energy, which has opposite sign of the anharmonicity.

The applied flux Φ that threads the j^{th} SQUID loop is generated when the i^{th} Z-line, which has mutual inductance with the SQUID loop, has current flowing through it. The applied current is proportional to the applied voltage V_i across a line impedance of 50Ω . The voltage range used to tune E_J allows the observation of one oscillating period of the resonator frequency in the dispersive readout without exceeding the critical current of the flux lines.

Given this intuition, Eq. (S3) and Eq. (S4) can be rewritten as [10]

$$f_{01}(V_i) = \left(f_{01,\max} + \frac{E_C}{h}\right) \times \sqrt{d^2 + [1 - d^2] \cos^2(A_c[V_i - V_{\text{ofs},i}])} - \frac{E_C}{h}, \quad (\text{S5})$$

where $f_{01,\max} = (\sqrt{8E_{J,\max} E_C} - E_C)/h$ is the frequency of the upper sweet spot, $-E_C/h$ is the anharmonicity, A_c is a conversion factor related to the mutual inductance between the i^{th} SQUID loop and the i^{th} flux line, and $V_{\text{ofs},i}$ is the offset voltage induced by remnant flux. Note that A_c and $V_{\text{ofs},i}$ are related to the normalized flux of the transmon by

$$A_c(V_i - V_{\text{ofs},i}) = \frac{\pi\Phi}{\Phi_0}, \quad (\text{S6})$$

We used the nominally designed junctions asymmetry noted in I. E_C is determined by the two-photon excitation experiment. Eq. (S5) is used to fit the peak frequencies obtained from the qubit and coupler spectra of

Figs.2(a-d) in the main text, with $f_{01,\max}$, $V_{\text{ofs},i}$ and A_c as fitting variables. Eq. (S6) is then used to calibrate the horizontal axis in Figs.2(a-d) according to its normalized flux response.

As two-qubit gate operations require accurate idling of the qubit and coupler frequencies away from the upper sweet spot, it is essential to determine the precise bias voltage. Solving the bias voltage as a function of f_{01} from Eq. (S5), the idle flux bias can be written as

$$V_{\text{idle}}(f_{01}) = V_{\text{ofs},i} \pm \frac{1}{2A_c} \times \arccos\left(\frac{2}{1 - d^2} \left[\frac{f_{01} + E_C/h}{f_{01,\max} + E_C/h}\right]^4 - \frac{1 + d^2}{1 - d^2}\right). \quad (\text{S7})$$

Eq. (S7) helps determine idle voltages through an idle qubit and coupler frequencies that enable 2Q gates like the iSWAP gate and the conditional phase (CZ) gate.

B. Ramsey-based Protocol

Figs. 3(a) of the main text and the inset of Figure S2 show the MZLC and Ramsey-based pulse sequences, respectively. Both are used to measure flux crosstalk. In both methods, voltages are applied simultaneously to the detector Z-line and a source Z-line. The detector voltage is then adjusted to maintain a constant transition frequency, effectively nullifying the net flux through the detector element. Both source and detector voltages are converted into flux quanta to intuitively link the experiment to the transmon picture.

The two approaches differ only in the frequency extraction method. MZLC utilizes two-tone spectroscopy overlapping with probe and source voltages, while the Ramsey-based approach employs Ramsey interferometry, which outputs oscillating patterns shown in Fig. S2(a). MZLS has good contrast for low readout SNR measurements and is robust against decoherence. The drawback of this method lies in its sensitivity to higher-order flux noise and the Purcell effect near the sweet spot frequency.

Meanwhile, the Ramsey-based method has increased sensitivity to frequency detuning induced by different probe bias ranges, leading to more precise flux-crosstalk measurement, as shown from Fig. S2(b). This measurement is limited by the qubit dephasing time. For the two-tone approach, both qubits are susceptible to dephasing due to an excess $|1\rangle$ population due to incomplete thermalization of the qubit and spurious excitation from the rectangular readout pulse.

C. Flux Crosstalk Compensation Scheme

The procedure for flux crosstalk cancellation has three steps. First, we measure the transition frequencies of all

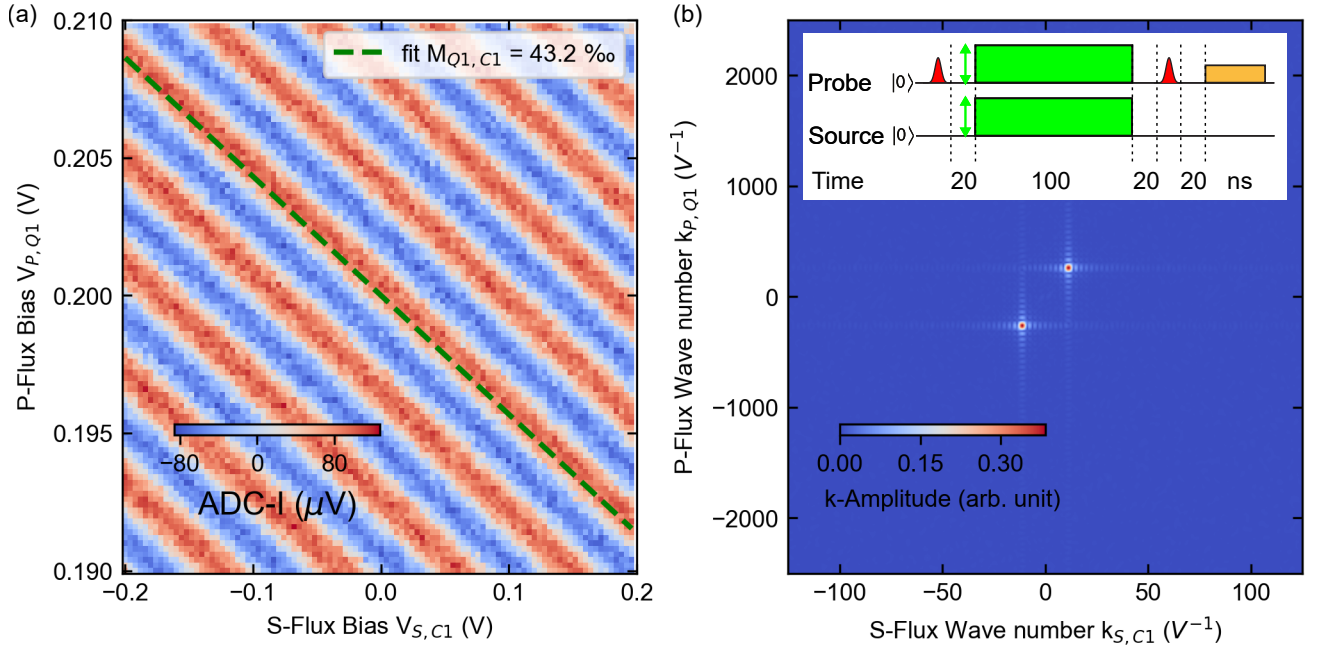


FIG. S2. Characterizing magnetic flux crosstalk by resolving Ramsey Oscillations (a). By performing the 2D-FFT of the Ramsey fringes as shown in (b), we determine the perpendicular crosstalk. Inset shows the pulse schedule used to detect the flux crosstalk via Ramsey interferometry. By obtaining an orthogonal slope from the two points, we measure the flux crosstalk, which translates to a green-dashed line in (a).

tunable qubits and couplers. Second, we quantify the crosstalk between a source Z-line and nearby detector elements. Finally, we construct a crosstalk cancellation matrix that enables effective multi-Z-line control.

Flux crosstalk arises from mutual inductive coupling between the flux lines (Z-lines) and the superconducting loops of nearby qubits or couplers. The mutual inductance matrix L represents these sets of inductances and maps the vector of the Z-line current, represented as a matrix I_Z , to the vector of induced fluxes as follows:

$$\Phi = L \cdot I_Z. \quad (\text{S8})$$

Current is generated from the applied voltage V_Z across a 50Ω impedance of the Z-line. Generating all currents in the subsystem makes up an applied voltage matrix V_Z , we define an effective mutual inductance matrix M accounting for the resistance and line response such that:

$$\Phi = M \cdot V_Z. \quad (\text{S9})$$

Since our goal is to cancel the undesired flux threading a detector SQUID loop, the absolute scaling in M is irrelevant. We then normalize each row of M by its diagonal entry M_{ii} , resulting a dimensionless crosstalk matrix X :

$$V_{\text{eff}} = X \cdot V_Z. \quad (\text{S10})$$

We are concerned about the voltage change ΔV_{Z_i} required on the Z-line i to compensate for the flux induced by a voltage change ΔV_{Z_k} on the Z-line k . We expect a vanishing net flux between flux lines:

$$\Phi_i = M_{ii}\Delta V_{Z_i} + M_{ik}\Delta V_{Z_k} = 0. \quad (\text{S11})$$

The solution for Eq. (S11) defines an element in the flux crosstalk matrix X :

$$X_{ik} = \frac{M_{ik}}{M_{ii}} = -\frac{\Delta V_{Z_i}}{\Delta V_{Z_k}}. \quad (\text{S12})$$

In summary, all diagonal elements of X are equal to 1 ($X_{ii} = 1$), and the off-diagonal elements $X_{ik, i \neq k}$, quantify the fraction of compensation voltage required on the Z-line i to cancel the flux induced by the Z-line j . This formulation provides a simple and intuitive picture of flux crosstalk, directly in terms of the applied voltages. X is characterized by both characterization protocols as shown in Fig. 4(a,b) of the main text with its absolute magnitude represented in Fig. S3(a,b).

To eliminate flux crosstalk, we compute the inverse of this matrix, X^{-1} , and use it to define a *cancellation matrix* that maps the target bias voltages back to physical control voltages:

$$V_Z = X^{-1} \cdot V_{\text{target}}. \quad (\text{S13})$$

By applying these compensated voltages to the Z-lines, each tunable element can be independently biased, ensuring that off-diagonal flux contributions are suppressed. The effectiveness of the cancellation is verified by remeasuring the crosstalk matrix after compensation and confirming that it approximates the identity matrix as shown in Fig. 4(c) in the main text, and its absolute magnitude in Fig. S3(c).

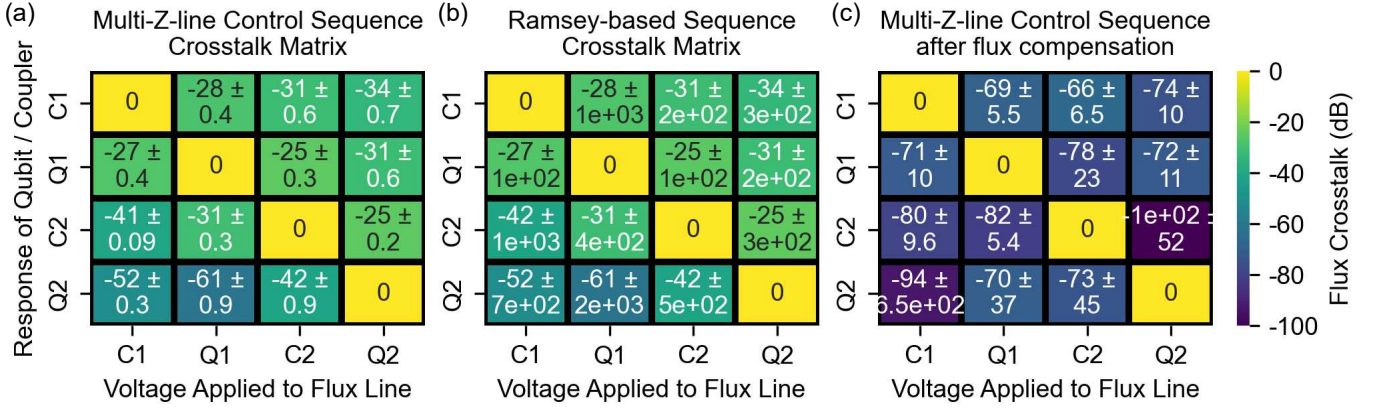


FIG. S3. Crosstalk matrices X in the main-text but now expressed in dB.

D. Mapping between Coupler-Mediated CZ Coupling Strength and Flux-Compensated Flux Bias

The CZ coupling strength in a transmon coupler architecture can then be written as [11]

$$g_{\text{eff}} = g_{02} = \sqrt{2} \left(g_{12} - \frac{g_{1c}g_{2c}}{2} B_{02} \right), \quad (\text{S14})$$

where g_{12} is the direct coupling between the qubits Q1 and Q2, g_{1c} is the coupling strength between the qubit Q1 and the coupler C2, g_{2c} is the coupling strength between Q2 and the coupler C2, and [11]

$$B_{02} = \frac{1}{\Delta_1} + \frac{1}{\Delta_2 - E_{C,2}/\hbar} + \frac{1}{\sum_1} + \frac{1}{\sum_2 + E_{C,2}/\hbar}. \quad (\text{S15})$$

In Eq. (S15), $\Delta_j = \omega_c - \omega_j$ where $\omega_c = 2\pi f_{01,c}$ is the coupler frequency and $\omega_j = 2\pi f_{01,j}$ is the frequencies of the j th qubit. $\sum_j = \omega_c + \omega_j$. The first term in Eq. (S15) represents the detuning between ω_c and idle ω_{01} of Q1 while the second term refers to the detuning between the coupler and the idle ω_{21} frequency of Q1. The third and fourth terms refer to the sum of the coupler frequency and the idle frequencies for the first and second qubits for CZ operation. Optimum values of Eq. (S15) occur when $\delta_{21} = 0$, when $\omega_1 = \omega_2 - E_{c,2}/\hbar$.

We then characterize the coupler-mediated coupling strength g_{eff} between states $|11\rangle$ and $|02\rangle$. Here, the first and second digits of the state vectors refer to the single-qubit state of Q1 and Q2, respectively. After preparing a $|11\rangle$ state, we apply a rectangular pulse with pulse duration $T = 100$ ns for both qubits and couplers. Assuming that the detuning δ_{21} between the $|11\rangle$ and $|02\rangle$ states has observable Rabi oscillations, the population of the $|11\rangle$ for two coupled qubits can be modelled as [12–14]

$$P_{|11\rangle \rightarrow |02\rangle}(\delta_{21}, g_{\text{eff}}, t) = \frac{2g_{\text{eff}}^2 [1 + \cos(D \times t\Omega(g_{\text{eff}}, \delta_{21}))]}{\Omega^2(g_{\text{eff}}, \delta_{21})}, \quad (\text{S16})$$

where t is the duration between diabatic pulses,

$$\Omega^2(g_{\text{eff}}, \delta_{21}) = 4g_{\text{eff}}^2 + \delta_{21}^2, \quad (\text{S17})$$

and D represents the reduced factor accounting the imperfect diabatic pulse shape experienced by the coupler. We model D as a ratio of a diabatic pulse with an effective rising pulse time t_{eff} to that of the ideal pulse shape area:

$$D = \frac{\int_0^T A + A_{\text{eff}} \times \exp(-t/t_{\text{eff}}) dt}{At}. \quad (\text{S18})$$

For Eq. (S18) to achieve a value $D = 0.16$, making Fig. 5(d) of the main text in excellent agreement with Fig. 5(c), we set $A_{\text{eff}} = -A$ and $t_{\text{eff}} = 278$ ns. This value of the time constant, though extracted empirically, accounts for both short and long time constants that were not corrected even after flux compensation. Eq. (S16) simulates the ideal CZ SWAP experiment at constant δ_{21} , and the CZ leakage at constant t .

Proper mapping between the idle voltage of the coupler V_c and the coupling strength g_{eff} is a key engineering trick to control the interaction strength between two qubits in a CZ gate operation. Note that the dependence between g_{eff} and δ_{21} can be traced on the idling of the second qubit in its $1 \rightarrow 2$ frequency

$$\omega_{01,2} = \delta_{21} + \omega_{01,1} + E_{c,2}/\hbar. \quad (\text{S19})$$

As $\omega_{01,2}$ are present in the second, third, and fourth term in Eq. (S15), solving for $\omega_{01,1}$ as functions of g_{eff} and δ_{21} becomes cumbersome, and require numerical routines. Once $\omega_{01,1}$ is solved, we use Eq. (S5) to express the coupler voltage as functions of g_{eff} and δ_{21} . Establishing its analytical form for intuition requires 1) precise control of parameters such as $\delta_{21} = 0$ so that $\omega_c - \omega = \Delta_1 = \Delta_2 - E_{C,2}/\hbar$ and 2) neglecting the third and fourth terms in Eq. (S15). These are valid for $\omega_c \gtrsim \omega$.

The simplifications made above rewrite Eq. (S14) and Eq. (S15) as

$$g_{\text{eff}} = \sqrt{2} \left(g_{12} - \frac{2g_{1c}g_{2c}}{\omega_c - \omega} \right). \quad (\text{S20})$$

By rearranging the terms to solve for $\omega_c = 2\pi f_{01,c}$ and plugging in Eq. (S5) to solve for $V_{\text{idle},c}$, the idle flux bias

of the coupler required to control the coupling strength in a CZ interaction can be written as

$$V_{\text{idle},c}(g_{\text{eff}}, \omega) = V_{\text{ofs},c} \pm \frac{1}{2A_{c,cj}} \times \arccos \left(\frac{2}{1 - d_c^2} [K(g_{\text{eff}}, \omega)]^4 - 1 \right), \quad (\text{S21})$$

where

$$K(g_{\text{eff}}, \omega) = \frac{\omega + \frac{2g_{1c}g_{2c}}{g_{12} - g_{\text{eff}}/\sqrt{2}} - E_{C,c}/\hbar}{\omega_{01,c,\text{max}} + E_{C,c}/\hbar}. \quad (\text{S22})$$

As Eq. (S21) and ω assume appropriate flux-crosstalk compensation for precise idling and control of the coupler-assisted coupling strength as established in the main text, flux-crosstalk compensation becomes a vital protocol in accurately setting not only the idle qubit frequencies in a two-qubit gate operation, but also in precise control of g_{eff} .

-
- [1] J. Wenner, M. Neeley, R. C. Bialczak, M. Lenander, E. Lucero, A. D. O'Connell, D. Sank, H. Wang, M. Weides, A. N. Cleland, *et al.*, Wirebond crosstalk and cavity modes in large chip mounts for superconducting qubits, *Supercond. Sci. Technol.* **24**, 065001 (2011).
 - [2] Y. Sung, *High-fidelity two-qubit gates and noise spectroscopy with superconducting qubits* (2022), PhD Thesis, Massachusetts Institute of Technology.
 - [3] A. V. Anferov, *Millimeter Wave Superconducting Quantum Devices* (2024), PhD Thesis, University of Chicago.
 - [4] A. Osman, J. Simon, A. Bengtsson, S. Kosen, P. Krantz, D. P. Lozano, M. Scigliuzzo, P. Delsing, J. Bylander, and A. Fadavi Roudsari, Simplified josephson-junction fabrication process for reproducibly high-performance superconducting qubits, *Appl. Phys. Lett.* **118**, 064002 (2021).
 - [5] C.-H. Liu, *Photon assisted quasiparticle poisoning and single flux quantum-based digital control of superconducting qubit* (2023).
 - [6] F. Arute, K. Arya, R. Babbush, D. Bacon, J. C. Bardin, R. Barends, R. Biswas, S. Boixo, F. Brandao, D. A. Buell, *et al.*, Quantum supremacy using a programmable superconducting processor, *Nature* **574**, 505 (2019).
 - [7] S. Krinner, S. Storz, P. Kurpiers, P. Magnard, J. Heinsoo, R. Keller, J. Lütolf, C. Eichler, and A. Wallraff, Engineering cryogenic setups for 100-qubit scale superconducting circuit systems, *EPJ Quantum Technol.* **6**, 1 (2019).
 - [8] Z. Chen, *Metrology of quantum control and measurement in superconducting qubits* (2018), PhD Thesis, University of California Santa Barbara.
 - [9] J. Koch, T. M. Yu, J. Gambetta, A. A. Houck, D. I. Schuster, J. Majer, M. H. Blais, Alexander; Devoret, S. M. Girvin, and R. J. Schoelkopf, Charge-insensitive qubit design derived from the Cooper pair box, *Phys. Rev. A* **76**, 042319 (2007).
 - [10] C. N. Barrett, A. H. Karamlou, S. E. Muschinske, I. T. Rosen, J. Braumüller, R. Das, D. K. Kim, B. M. Niedzielski, M. Schuldt, K. Serniak, *et al.*, Learning-Based Calibration of Flux Crosstalk in Transmon Qubit Arrays, *Phys. Rev. Appl.* **20**, 024070 (2023).
 - [11] E. A. Sete, N. Didier, A. Q. Chen, S. Kulshreshtha, R. Manenti, and S. Poletto, Parametric-Resonance Entangling Gates with a Tunable Coupler, *Phys. Rev. Appl.* **16**, 024050 (2021).
 - [12] Y. Sung, L. Ding, J. Braumüller, A. Vepsäläinen, B. Kannan, M. Kjaergaard, A. Greene, G. O. Samach, C. McNally, D. Kim, *et al.*, Realization of High-Fidelity CZ and ZZ-Free iSWAP Gates with a Tunable Coupler, *Phys. Rev. X* **11**, 021058 (2021).
 - [13] C. Hellings, N. Lacroix, A. Remm, R. Boell, J. Herrmann, S. Lazăr, S. Krinner, F. Swiadek, C. K. Andersen, C. Eichler, *et al.*, *Calibrating Magnetic Flux Control in Superconducting Circuits by Compensating Distortions on Time Scales from Nanoseconds up to Tens of Microseconds* (2025), [arXiv:2503.04610 \[quant-ph\]](https://arxiv.org/abs/2503.04610).
 - [14] C. Križan, J. Biznárová, L. Chen, E. Hogedal, A. Osman, C. W. Warren, S. Kosen, H.-X. Li, T. Abad, A. Aggarwal, *et al.*, Quantum SWAP gate realized with CZ and iSWAP gates in a superconducting architecture, *New J. Phys.* **27**, 074507 (2025).